

ManipGPT: Is Affordance Segmentation by Large Vision Models Enough for Articulated Object Manipulation?

Taewhan Kim, Hojin Bae, Zeming Li, Xiaoqi Li, Iaroslav Ponomarenko, Ruihai Wu, Hao Dong

Abstract—

Visual actionable affordance has emerged as a transformative approach in robotics, focusing on perceiving interaction areas prior to manipulation. Traditional methods rely on pixel sampling to identify successful interaction samples or processing pointclouds for affordance mapping. However, these approaches are computationally intensive and struggle to adapt to diverse and dynamic environments. This paper introduces ManipGPT, a framework designed to predict optimal interaction areas for articulated objects using a large pre-trained vision transformer (ViT). We created a dataset of 9.9k simulated and real images to bridge the sim-to-real gap and enhance real-world applicability. By fine-tuning the vision transformer on this small dataset, we significantly improved part-level affordance segmentation, adapting the model’s in-context segmentation capabilities to robot manipulation scenarios. This enables effective manipulation across simulated and real-world environments by generating part-level affordance masks, paired with an impedance adaptation policy, sufficiently eliminating the need for complex datasets or perception systems.

Index Terms—Perception for Grasping and Manipulation, Object Detection, Segmentation and Categorization

I. INTRODUCTION

Robotic manipulation is crucial for enabling robots to perform in wide variety of tasks autonomously. Despite its importance, it remains a complex and challenging problem largely due to the variability in objects, environments, and required actions.

A promising approach to address this challenge is visual actionable affordance, which reframes robotic manipulation as a perception task. This method uses visual cues to predict optimal interaction points, streamlining manipulation tasks. Traditional affordance map generation [1]–[3] involves sampling pixels on an object, interacting at each point, and recording scores to construct a map. This process is repetitive, computationally intensive, and further burdened by reliance on point cloud data. Additionally, the interaction data collected in simulation often fails to translate seamlessly to real-world experiments due to physical differences, creating a significant sim-to-real gap.

Recent advancements leverage large-scale datasets, sophisticated perception algorithms, and large language models (LLMs) to enhance task execution [4], [5]. However, these methods often result in high computational costs and increased complexity, limiting their practicality in resource-constrained environments. Additionally, a gap between language and vision modalities hinders the seamless integration of visual and

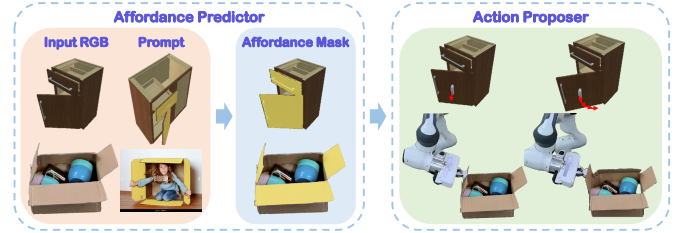


Fig. 1. ManipGPT processes an RGB image with a visual prompt to generate an affordance mask, which determines the contact point and manipulation direction.

language-based commands, affecting the execution of complex tasks.

To overcome these limitations, we present ManipGPT, a minimalist approach that leverages a fine-tuned large vision model in context to predict affordance masks for a wide range of indoor objects, significantly simplifying robotic manipulation. Our streamlined approach, using a single RGB image and a pair of prompt images to directly generate affordance masks, eliminates the need for iterative sampling techniques and enables one-shot manipulation without requiring robot-specific training. Additionally, we present a synthetic dataset of 9.9k images from both simulated and realistic environments, demonstrating that even minimal datasets with basic annotations can enhance robotic performance effectively.

Our system integrates affordance masks with a post-processing algorithm to ensure safe and efficient manipulation, including an optional impedance control mechanism for improved physical adaptability. Experimental results show that our framework predicts interaction points with human-like intuition, generating actionable affordance maps that enable robots to identify contact areas and motion directions efficiently. These findings suggest that our approach reduces computational complexity while maintaining or improving the accuracy of robotic manipulation, making it particularly valuable for resource-constrained applications.

The contributions of this paper are as follows:

- 1) We propose ManipGPT, a novel framework that utilizes an in-context large vision model to predict affordance masks for a diverse range of articulated and indoor objects, simplifying robotic manipulation tasks.
- 2) Our streamlined approach employs a single RGB image and a pair of prompt images to directly generate affordance masks, removing the need for robot-specific training.
- 3) We present a synthetic dataset of 9.9k images, combining simulated and realistic articulated objects, demon-

strating the framework’s efficiency in bridging the sim-to-real gap and enhancing robotic performance with minimal dataset requirements.

II. RELATED WORKS

A. Articulated Object Manipulation

Articulated object manipulation poses significant challenges due to geometric variability and the interactive nature of object parts. Existing methods largely fall into two categories: affordance-based policies and articulation estimation.

Affordance-based policies actionable regions on objects by generating affordance maps that indicate the likelihood of moving object parts [1]–[3], [6]. While these methods offer generalization to novel objects, these methods typically involve a dataset collection stage where the robot iteratively samples points in a point cloud or pixels in an image to interact with the object, aiming to identify the most actionable regions. This process is time-consuming and computationally intensive, especially in a 3D simulation environment. Moreover, the reliance on simulations introduces a sim-to-real gap, meaning the affordance map collected from simulated interactions may not accurately reflect real-world scenarios.

Articulation estimation methods, on the other hand, predict 6D joint parameters directly from visual inputs such as a sequence of images [7], [8], RGB-D images [9], [10], or point clouds [11], [12]. By segmenting images or point clouds and estimating part poses, these methods enable robust manipulation trajectories.

In contrast, our approach simplifies the process by using a single RGB image and prompt inputs to generate an affordance mask. This eliminates the need for pointclouds or iterative sampling for affordance learning and achieves effective manipulation with minimal computational overhead.

B. Large Models and Applications in Robotics

Recent advancements in large vision models [13]–[15] have revolutionized semantic and instance segmentation. These models, enable robots to adapt to diverse environments with minimal real-world training. By leveraging pre-trained models, robots can rapidly adapt to new real-world scenarios, enhancing their operational efficiency. In robotics, These vision models are crucial for tasks requiring detailed visual representations, such as point cloud and 2D image segmentation [16], [17].

Large Language Models (LLMs) like GPT [18] and LLaMA [19] further enhanced robotics by enabling natural language understanding, complex task execution, and advanced reasoning capabilities. These models bridge the gap between abstract knowledge and physical actions by integrating with other modalities like visual perception, allowing robots to perform context-aware and adaptive manipulations. Their integration with Visual Language Models (VLMs) enables context-aware reasoning and adaptive task execution from language-based commands [4], [5].

While large vision models have widely been used as supplementary tools for pre-processing or post-processing, with LLMs serving as the backbone, our approach diverges by implementing SegGPT [14] as the primary backbone

model. Unlike resource-intensive LLMs, SegGPT’s efficient 370 million parameter architecture offers vivid segmentation and flexible visual prompting, making it ideal for resource-constrained applications.

C. 2D Affordance Datasets

Several key datasets have been developed to enhance the understanding of object affordance in robotic manipulation.

HANDAL [20]: This dataset targets category-level pose estimation and affordance prediction, emphasizing hardware and kitchen environments to support precise robotic object handling in real-world applications.

AGD20K [21]: A large-scale dataset for affordance grounding tasks, featuring images annotated with actionable regions on objects, such as gripping or cutting areas.

IIT-AFF [22]: Specializes in affordance classification for kitchen utensils, offering detailed part segmentation for specific cooking-related actions.

These datasets primarily focus on small, hand-held tools with interaction annotations, posing challenges for robots in learning and applying affordances to more complex, articulated objects, which limits their applicability in broader robotic manipulation tasks.

III. METHOD

Our framework is divided into two key modules: the Affordance Predictor and the Action Proposer. The model-based Affordance Predictor generates an affordance mask from an RGB input, while the algorithm-based Action Proposer identifies the optimal grasping spot, initial manipulation direction, and subsequent action directions.

A. Affordance Predictor

Our affordance predictor generates part-level affordance masks for articulated objects. Guided by a single pair of category-specific visual prompts, it produces high-precision affordance masks. As illustrated in Figure 2(a), the target RGB image of a cabinet, along with the visual prompt of the category, are input into the model. Leveraging the visual prompt’s resembling features, the model generates an accurate affordance mask as depicted in Figure 2(b).

In real robot experiments, we refined multi-part masks using SAM [13], while simulations used built-in segmentation to select a single part. For consistency in our experiments, the largest part mask was chosen to manipulate. The selected mask is then used to calculate the center spot, ensuring that the gripper is positioned in a safe zone, where physical restrictions are not a concern.

B. Action Proposer

After determining the actionable point, the next step is to translate these visual cues into physical manipulation. We achieve this by utilizing the surface normal vector derived from the masked region. These normal vectors provide crucial information about the surface orientation of the object, which is essential for determining the optimal grasping pose and manipulation direction. Since the gripper operates perpendicular to the surface at the contact point, the model can either pull or push the articulated object.

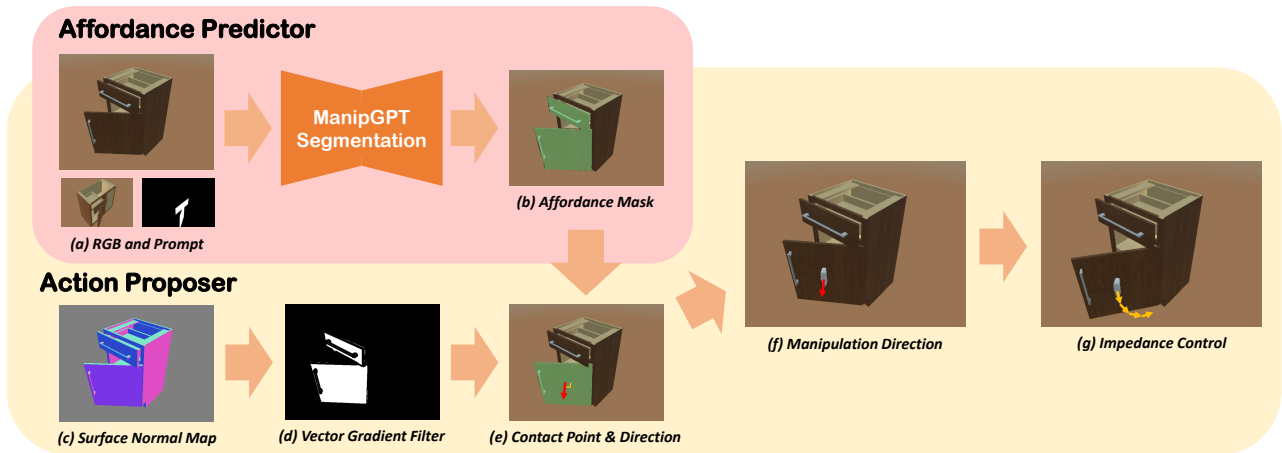


Fig. 2. The pipeline is divided into two main modules: Affordance Predictor and Action Proposer. (a) The RGB image and category-specific prompt are input to generate an affordance mask. (b) The affordance mask highlights actionable parts of the object. (c) A surface normal map is used to understand the object’s surface orientation. (d) A vector gradient filter refines the normal map by filtering out non-ideal areas. (e) The optimal contact point and manipulation direction are identified. (f) The manipulation direction is set for the gripper’s action. (g) An impedance control algorithm guides the robot’s manipulation based on physical feedback.

In cases where the normal vector and the contact point are obtained on an uneven surface, we apply a gradient filtering on the normal map to filter out non-smooth surfaces and identify a safe contact point and manipulation direction in Algorithm 1. In the case of storage furniture where the top drawer has a cylindrical handle in the center shown in Figure 2(d), the normal vector on the region is not ideal for identifying a grasping spot. By filtering through the vector gradient, we can locate a safer area for determining the grasping pose, grasping area, and manipulation direction.

The remaining manipulation steps are executed using an active impedance control algorithm of [5]. This algorithm allows for precise control over the robot’s movements, particularly when interacting with revolute joints. By adopting a step-by-step approach, the robot can adjust its grip and movement in real-time, responding to the physical feedback it encounters. This method is crucial for enabling the robot to adapt to various object shapes and sizes, as well as to the articulated movements of objects with multiple joints.

IV. DATASET

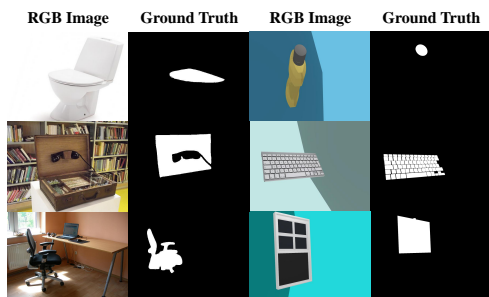


Fig. 3. Sample RGB images and ground truth affordance masks: real-world examples (left) and simulated images (right). White regions indicate manipulable affordance areas.

We constructed a dataset tailored for affordance detection

in robotic manipulation, comprising 13,350 images across 30 object categories—18 for training and 12 for testing. The dataset integrates simulated and real-world images to ensure robustness and adaptability, as shown in Figure 3.

Training Data: The training set includes 9,900 images: 9,000 simulated images generated in the SAPIEN environment [23] and 900 real-world images. Simulated data spans 18 categories, with 5 objects per category and 100 articulation steps captured from random angles ($5 \times 100 \times 18$). Real-world images, sourced from ImageNet [24], COCO [25], OpenImagesV7 [26], MyNursingHome [27], Pixabay [28], and our own captures, include 50 images per category.

Testing Data: The test set comprises 3,450 images: 3,000 simulated images sampled from random viewpoints and articulations of novel instances and 450 real-world images. Real-world images were annotated using CVAT.ai [29], while simulated annotations were automatically derived from actionable link IDs.

Annotation criteria ensure masks encompass the manipulable parts, focusing where a robot can attach and interact. Minor overlaps with non-relevant surfaces are permitted if the primary focus remains on the manipulable part.

By combining controlled simulated environments with diverse real-world data, this dataset provides a foundation for advancing affordance detection in manipulation.

V. EXPERIMENT

A. Training Details

The fine-tuning process was crucial for adapting our backbone model from a general segmentation framework to a specialist in part-level affordance detection, enabling a robot arm to approach and execute precise manipulations. We trained the model for 300 epochs with a learning rate of $1e-5$, keeping all other hyper-parameters identical to those of the backbone model, including the L1 loss function. The training was conducted on a single A800 80G GPU.

Algorithm 1 Finding contact point and direction for manipulation

Input: Normal map N_{map} , part mask M_{part}

Output: Contact point (x, y) , manipulation direction \mathbf{n}

- 1: Apply gaussian blur to smooth the normal map N_{map} .
 - 2: Split the normal map N_{map} into x, y, and z components (N_x, N_y, N_z) and compute gradients ∇_x , ∇_y , and ∇_z .
 - 3: Calculate the gradient magnitude $G_{mag} = \sqrt{\nabla_x^2 + \nabla_y^2 + \nabla_z^2}$.
 - 4: Generate edge mask M_{edge} by thresholding G_{mag} with a predefined filter value.
 - 5: Multiply inverted M_{edge} by M_{part} to create $M_{invedge}$, a mask for flat surfaces.
 - 6: Apply $M_{invedge}$ to the original normal map N_{map} to obtain the masked normal map N_{masked} .
 - 7: Compute the centroid (c_x, c_y) of M_{part} .
 - 8: **if** $(c_x, c_y) \in N_{masked}$ **and** $N_{masked}(c_x, c_y) \neq [0, 0, 0]$ **then**
 - 9: Set the contact point $(x, y) = (c_x, c_y)$.
 - 10: Set the manipulation direction \mathbf{n} to the normal vector at (c_x, c_y) .
 - 11: **else**
 - 12: Set the manipulation direction \mathbf{n} to the most frequent non-zero normal vector in N_{masked} .
 - 13: **if** $N_{masked}(c_x, c_y) = [0, 0, 0]$ **then**
 - 14: Define a centered bounding box B with one-third dimensions of M_{part} around (c_x, c_y) .
 - 15: **if** $\forall(x, y) \in B, N_{masked}(x, y) \neq [0, 0, 0]$ **then**
 - 16: Set (x, y) to a random non-zero pixel in B .
 - 17: **else**
 - 18: Set (x, y) to a random non-zero pixel in M_{part} .
 - 19: **end if**
 - 20: **end if**
 - 21: **end if**
 - 22: **return** (x, y) , \mathbf{n}
-

For in-context tuning, we created specific prompts for 30 categories outside our dataset. These prompts were designed to help the model better identify affordance regions in a variety of objects. For each category, we used one real image and one simulation image as prompts to test the model on both real and simulated data.

TABLE I

THIS IS THE SEGMENTATION RESULT ON SIMULATED AND REAL IMAGES.

""*"" INDICATES TEST RESULT ON REAL IMAGES ONLY.

Method	mIoU	F ₁ score	mIoU*	F ₁ score*
ViT	34.1	37.2	14.8	26.0
Bayesian	47.0	56.9	55.5	65.0
SegGPT	34.9	56.0	36.2	45.1
LISA	46.3	56.2	40.1	49.1
Ours	66.5	74.5	73.4	80.3

B. Affordance Segmentation Experiment and Baselines

We evaluated our model’s performance against several segmentation baselines, summarized as follows:

- **Vision Transformer:** Inspired by [30], our custom ViT model divides images into 16×16 patches, encoding each patch into a 768-dimensional vector. These vectors are processed through 12 attention blocks, each with 8 attention heads and a multi-layer perceptron. The model was trained for 500 epochs using a cross-entropy loss function, with an initial learning rate of 4e-5 and a dropout rate of 0.2.
- **Bayesian** [31]: Using ResNet-50 blocks, this model identifies multiple affordance masks within a single image. We adapted it to detect a single-class affordance mask, training it on our dataset without modifying its original hyperparameters.
- **LISA** [32]: A multi-modal, language-prompted segmentation model with advanced reasoning capabilities. LISA can segment various elements, including affordance masks, using natural language prompts. Since it requires a language dataset and is already pre-trained for part segmentation, we tested LISA without additional fine-tuning to assess the performance of language-prompted segmentation against image-prompted approaches.
- **SegGPT** [14]: Serving as the backbone of our model, SegGPT was tested in its pre-trained state to benchmark its affordance segmentation performance. This comparison highlights the extent of improvement achieved by our fine-tuning approach.

C. Baseline Comparison and Analysis

The vanilla ViT, due to its small scale, showed rapid loss reduction during training, but it struggled to generalize to unseen categories, particularly in real-world images. This limitation made it less suitable for real-world applications.

Similarly, the limited variety of training categories constrained the Bayesian model’s segmentation ability, even though it achieved precise segmentation on its test set. Training the Bayesian model from scratch would require substantial data collection and computational resources, which led to poorer performance compared to ManipGPT when using the same training set.

Despite the use of carefully designed language prompts to guide segmentation, LISA’s performance fell short compared to both ManipGPT and SegGPT. For instance, when given the prompt “segment all flaps or wings of the box,” LISA often misinterpreted the instruction, segmenting the entire box instead of the specified parts. This highlights a limitation of language prompts in providing precise guidance for vision tasks, where ambiguity in language can lead to errors. In contrast, image prompts inherently offer a clearer and more aligned context for segmentation, avoiding the challenges posed by modality switching from language to vision.

Ours outperformed all other models. As shown in Table I, it achieved higher mean Intersection over Union (mIoU) and F1-scores on both simulated and real test images. By fine-tuning on a small set of images and leveraging SegGPT’s pre-trained checkpoints, ManipGPT excelled in affordance mask segmentation, demonstrating superior generalization and accuracy in real-world scenarios.

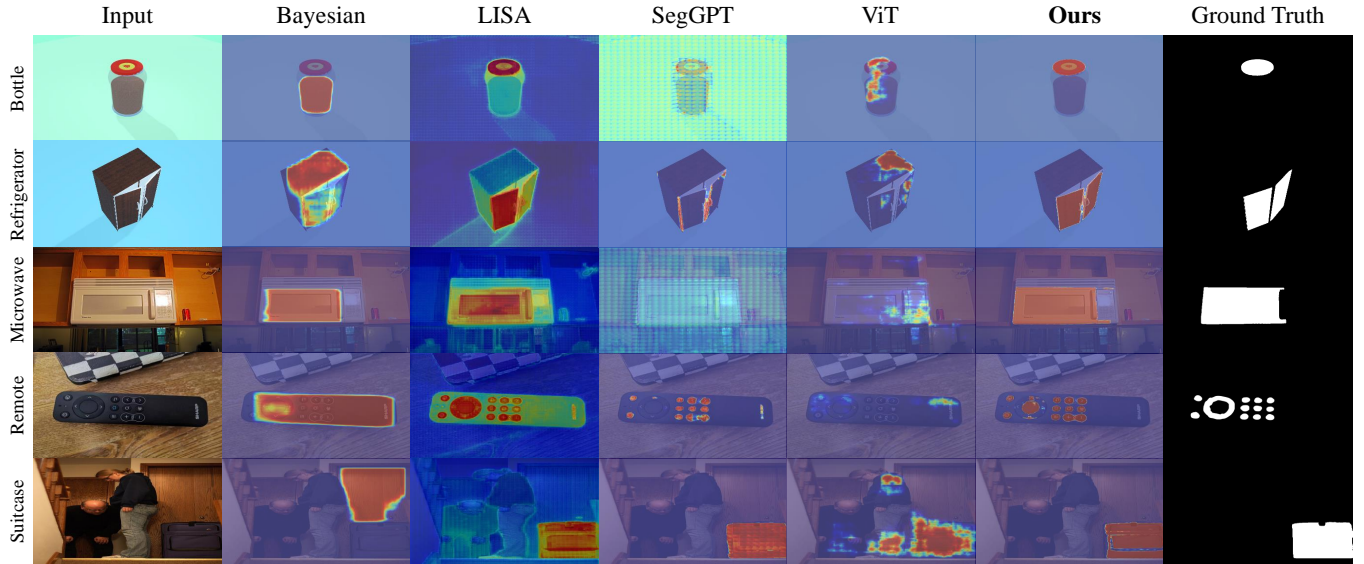


Fig. 4. Thermal map comparison of ManipGPT and other models. LISA struggled to mask out all actionable parts for certain categories, such as doors. Other models are lacked of generalization ability.

TABLE II

COMPARISON OF OUR METHOD AGAINST BASELINE MODELS. ‘OURS (RANDOM)’ REFERS TO THE RANDOM POINT POLICY, WHILE ‘OURS (LONG)’ REFERS TO MULTI-STEP MANIPULATION. ALL OTHER METHODS WERE EVALUATED USING ONE-STEP MANIPULATION.

Method	Novel Instances in Train Categories															
UMPNet	0.03	0.07	0.52	0.02	0.00	0.19	0.44	0.00	0.21	0.08	0.47	0.00	0.00	0.04	0.00	0.06
FlowBot3D	0.24	0.16	0.85	0.03	0.60	0.62	0.79	0.50	0.55	0.03	0.85	0.38	0.27	0.08	0.00	0.34
3DImplicit	0.18	0.11	0.45	0.08	0.00	0.45	0.45	0.10	0.34	0.05	0.50	0.00	0.09	0.16	0.00	0.08
ManipLLM	0.13	0.21	0.70	0.02	0.12	0.38	0.11	0.17	0.11	0.01	0.45	0.00	0.23	0.08	0.31	0.15
Ours	0.50	0.47	0.29	0.34	0.46	0.78	0.47	0.75	0.40	0.72	0.63	0.50	0.76	0.32	0.31	0.55
Ours(random)	0.43	0.29	0.69	0.21	0.68	0.69	0.54	0.58	0.33	0.45	0.53	0.75	0.76	0.33	0.69	0.49
Ours (long)	0.63	0.42	0.52	0.45	0.71	0.86	0.63	0.75	0.66	0.69	0.70	0.75	0.82	0.34	0.63	0.60

Method	Test Categories															
			AVG													AVG
UMPNet	0.30	0.10	0.14	0.56	0.15	0.07	0.02	0.00	0.13	0.50	0.63	0.13	0.07	0.33	0.17	0.23
FlowBot3D	0.76	0.40	0.41	0.79	0.17	0.21	0.29	0.03	0.13	0.88	0.91	0.53	0.26	0.66	0.57	0.45
3DImplicit	0.55	0.18	0.21	0.38	0.17	0.25	0.09	0.04	0.18	0.55	0.62	0.45	0.10	0.33	0.19	0.28
ManipLLM	0.55	0.25	0.22	0.69	0.20	0.16	0.04	0.03	0.08	0.41	0.41	0.49	0.19	0.47	0.50	0.31
Ours	0.80	0.43	0.53	0.88	0.23	0.77	0.38	0.11	0.73	0.88	0.80	0.35	0.52	0.64	0.58	0.57
Ours(random)	0.59	0.29	0.56	0.69	0.14	0.53	0.45	0.16	0.48	0.77	0.60	0.62	0.46	0.52	0.36	0.48
Ours (long)	0.88	0.63	0.65	0.94	0.36	0.89	0.65	0.30	0.86	0.94	0.88	0.46	0.52	0.69	0.61	0.68

D. Simulation Experiment and Baselines

The affordance predictor was evaluated against image segmentation baselines, while the action proposer was evaluated in conjunction with it. Before executing actions, we measured the Union False Positive Ratio (FPR_{Union}) to assess the accuracy of our model’s affordance masks. If the FPR_{Union} exceeded 0.5—indicating a significant amount of incorrectly masked area outside the ground truth—the manipulation attempt was skipped, and the instance was marked as a failure. The FPR is calculated as:

$$FPR_{Union} = \frac{\text{False Positives}}{\text{Predicted Mask} \cup \text{Ground Truth Mask}} \quad (1)$$

For the simulation, we tested pull motions—such as lifting

lids, opening doors, and pulling drawers—using a suction gripper in the SAPIEN simulation environment [23] and articulated objects from PartNet-Mobility [33]. The experiments included both one-step and multi-step manipulations:

- **One-step Manipulation:** The robot pulled 0.18 units in the direction proposed by the action proposer. Success thresholds were 0.1 units for prismatic joints and 0.1 radians for revolute joints.
- **Multi-step Manipulation:** The robot performed seven steps, each moving 0.05 units, with impedance control applied after each step. Success thresholds were set at 0.3 units and 0.3 radians.

We further analyzed our framework by testing it without

post-processing by selecting a random point within the affordance mask for grasping and pulling directions. This "random-point" policy was evaluated using the same criteria as the one-step manipulation.

The comparison against four baselines is as follows, with all models using the same simulation environment and end-effector:

- **UMPNet** [3]: Predicts closed-loop action sequences for manipulating articulated objects from RGB-D images, leveraging the "Arrow-of-Time" concept for goal-conditioned, multi-step manipulation. It uses two components: DistNet, which predicts contact points and manipulation directions, and AoTNet, which determines whether the action advances or reverses the object's state. We implemented both for comparison in our experiments.
- **Flowbot3D** [6]: Uses a 3D Articulation Flow (3DAF) vector field to predict point-wise motion directions. The ArtFlowNet model selects the interaction point based on the largest flow magnitude and the corresponding direction for end-effector positioning.
- **Implicit3D** [34]: Extends the 2D Transporter model to 3D, discovering temporally consistent keypoints in point cloud sequences. We used its 3D keypoints to determine the end-effector's pose.
- **ManipLLM** [5]: A multi-modal system using a language prompt and RGB image to predict the end-effector's pose through a structured chain-of-thought process. Once initial contact is established, subsequent waypoints are dynamically planned using active impedance adaptation.

E. Quantitative Evaluation in Simulator

Following the settings from ManipLLM [5], the baseline evaluation focused on the initial movement phase, which is crucial for assessing a model's ability to understand and respond to an object's initial state—key for successful long distance manipulation. All models were trained on a standardized dataset of 5 objects per category across 18 categories and evaluated under the same conditions. For ManipLLM, we used its pretrained model as it was trained on a larger set of objects and affordance data than ours. As a result, the train and test categories in Table II are not directly comparable, and the results reflect ManipLLM's generalization capability rather than performance on our dataset.

The results in Table II reveal that our approach consistently achieves high success rates, averaging 52.7% on seen and 57.3% on unseen object categories. This highlights its strong generalization capability, even for unfamiliar objects. Such success can be attributed to the effective use of visual cues, robust affordance segmentation, and the pre-trained vision transformer fine-tuned with minimal data.












The random-point policy, where the robot selects a random action point within the affordance mask, achieved a 52.8% success rate on average. However, this approach is less effective for real-world applications, as points on protruding features (e.g. handles) or near revolving joints (e.g. door hinges) often lead to poor attachment or excessive force during manipulation, reducing success rates for certain categories.



Fig. 5. We tested 11 objects in our real-world experiment, numbered 1–11 as listed in Table III. Objects 1–6 belong to the pushing category, while 7–11 are in the pulling category.

Multi-step manipulations demonstrated the highest success rates, achieving 65% on training categories and 68% on test categories. This underscores the value of impedance control in handling a variety of articulated objects, highlighting the robustness and adaptability of our algorithm.

TABLE III
REAL WORLD EXPERIMENTS FOR PUSHING AND PULLING CATEGORIES.

Pushing Categories						
Object Category						
Success/Total	5/6	3/6	6/6	5/6	4/6	5/6
Distance(m)	0.01	0.11	0.01	0.12	0.02	0.18
Pulling Categories						
Object Category						Avg
Success/Total	5/6	6/6	6/6	5/6	5/6	5/6
Distance(m)	0.23	0.09	0.15	0.16	0.18	0.11

F. Quantitative Evaluation in Real-world

We evaluated our framework in a real-world scenario where a real robot arm interacted with actual objects. The experiment included five pulling object categories and six pushing object categories, with two objects per category, each tested three times, resulting in six repetitions per category. RGB images and depth maps were captured using a RealSense D415 camera, and our model was used to predict affordances, which were then projected into 3D space. We implemented the Franka Emika Panda robot for the experiment. Since the robot originally had a parallel finger gripper, we modified it into a sticky gripper by closing the fingers and attaching double-sided foam tape around them. This adaptation allowed the

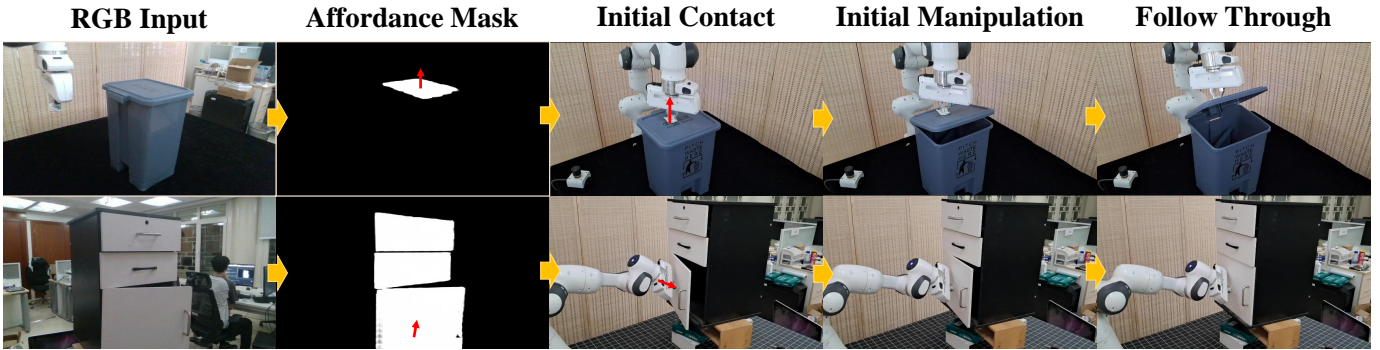


Fig. 6. This figure demonstrates the real object experiment. Above and below show pulling and pushing manipulation, respectively.

gripper to function similarly to a suction gripper, mimicking the simulation environment. Although the tape did not have sufficient adhesive strength to hold heavy objects for extended periods, it was durable enough to demonstrate our framework’s performance.

The results of real-world experiment are provided in Table III. We observe that our method shows no significant sim-to-real gap thanks to the synthetic image dataset. The model achieves a high success rate, excelling particularly in manipulating objects with well-defined boundaries and low actuation force requirements, such as boxes or keyboards. However, it occasionally struggles with objects featuring transparent or small targets like dispensers, or those with ambiguous boundaries like staplers. Additionally, accurate segmentation affordance for monitors can be challenging due to light reflections on the screen.

As we tested the simulation using simulated prompts and the real world using real image prompts, the real-world visualization in Figure 6 demonstrates that our model can successfully generalize to real-world robotic scenarios.

TABLE IV

ALL MODELS WERE TESTED ON REAL IMAGES ONLY. ”*” INDICATES OUR MODEL TRAINED ONLY ON SIMULATED IMAGES.

Model	SegGPT	Ours*	Ours
F₁ score	45.1	49.2	80.3
mIoU	36.2	40.2	73.4

G. Ablation Study

Our ablation study investigates the impact of including real images in the training set. We compared three configurations: SegGPT, ManipGPT trained only on SAPIEN images, and ManipGPT trained with both real and SAPIEN images.

Table IV shows that even a small number of real images significantly enhance SegGPT’s generalization ability for affordance segmentation. Specifically, including real images in the training set led to a 31.1% increase in the F₁ score and a 33.2% increase in the mIoU value. Given the importance of real-world images for manipulation tasks, our results strongly demonstrate the effectiveness of incorporating real data into the training process for real-world applications.

H. Limitations and failure cases

Our framework occasionally fails to produce masks, particularly with small objects or novel viewpoints. This is likely due to limited training data or ambiguity between the prompt image and the scenario image. To mitigate this, increasing the training dataset or adopting a few-shot learning approach with multiple prompts could enhance feature learning and improve mask accuracy. Additionally, the model’s reliance on one-shot prompts limits its effectiveness for unseen categories especially when a corresponding prompt image is unavailable. Developing a method to select optimal prompts from a database based on similarity could address this limitation.

Another challenge arises with transparent objects, such as kitchen pot lids, where their transparency hinders both segmentation and normal map acquisition, leading to lower success rates, as observed with the ‘Kitchen Pot’ category in Table II. One potential solution is to train models on video data, as the temporal consistency across frames could help disambiguate segmentation and provide more context for handling such objects.

Selecting optimal manipulation points also remains challenging. Although our approach targets the center of the masked region after filtering, it doesn’t always ensure the highest success rate, particularly with heavy objects and revolute joints. Using more detailed prompts with annotated manipulation points could improve accuracy.

VI. CONCLUSION

In this study, we present a comprehensive approach to robotic manipulation that integrates in-context vision with responsive robotic control. By fine-tuning a large vision model with a specialized dataset and leveraging normal vectors for interaction guidance, our system can effectively handle complex manipulation tasks. The approach simplifies the process by using a single RGB image and a pair of prompt images to directly generate affordance masks, removing the need for iterative sampling techniques. Additionally, our synthetic dataset of simulated and realistic images of articulated objects enhances the robot’s performance with minimal data. The results demonstrate significant advancements in affordance prediction, enabling the robot to identify contact areas and motion directions for precise manipulation. This streamlined framework is especially valuable for creating cost-effective,

adaptable robotic systems in resource-constrained environments.

REFERENCES

- [1] K. Mo, L. J. Guibas, M. Mukadam, A. Gupta, and S. Tulsiani, "Where2act: From pixels to actions for articulated 3d objects," in *Proceedings of the IEEE/CVF International Conference on Computer Vision*, 2021, pp. 6813–6823.
- [2] R. Wu, Y. Zhao, K. Mo, Z. Guo, Y. Wang, T. Wu, Q. Fan, X. Chen, L. Guibas, and H. Dong, "Vat-mart: Learning visual action trajectory proposals for manipulating 3d articulated objects," *arXiv preprint arXiv:2106.14440*, 2021.
- [3] Z. Xu, Z. He, and S. Song, "Universal manipulation policy network for articulated objects," *IEEE robotics and automation letters*, vol. 7, no. 2, pp. 2447–2454, 2022.
- [4] W. Huang, C. Wang, R. Zhang, Y. Li, J. Wu, and L. Fei-Fei, "Voxposer: Composable 3d value maps for robotic manipulation with language models," *arXiv preprint arXiv:2307.05973*, 2023.
- [5] X. Li, M. Zhang, Y. Geng, H. Geng, Y. Long, Y. Shen, R. Zhang, J. Liu, and H. Dong, "Manipllm: Embodied multimodal large language model for object-centric robotic manipulation," in *Proceedings of the IEEE/CVF Conference on Computer Vision and Pattern Recognition*, 2024, pp. 18 061–18 070.
- [6] B. Eisner, H. Zhang, and D. Held, "Flowbot3d: Learning 3d articulation flow to manipulate articulated objects," *arXiv preprint arXiv:2205.04382*, 2022.
- [7] A. Jain, R. Lioutikov, C. Chuck, and S. Niekum, "Screwnet: Category-independent articulation model estimation from depth images using screw theory," in *2021 IEEE International Conference on Robotics and Automation (ICRA)*. IEEE, 2021, pp. 13 670–13 677.
- [8] Z. Jiang, C.-C. Hsu, and Y. Zhu, "Ditto: Building digital twins of articulated objects from interaction," in *Proceedings of the IEEE/CVF Conference on Computer Vision and Pattern Recognition*, 2022, pp. 5616–5626.
- [9] N. Heppert, T. Migimatsu, B. Yi, C. Chen, and J. Bohg, "Category-independent articulated object tracking with factor graphs," in *2022 IEEE/RSJ International Conference on Intelligent Robots and Systems (IROS)*. IEEE, 2022, pp. 3800–3807.
- [10] V. Zeng, T. E. Lee, J. Liang, and O. Kroemer, "Visual identification of articulated object parts," in *2021 IEEE/RSJ International Conference on Intelligent Robots and Systems (IROS)*. IEEE, 2021, pp. 2443–2450.
- [11] L. Fu, R. Ishikawa, Y. Sato, and T. Oishi, "Capt: Category-level articulation estimation from a single point cloud using transformer," *arXiv preprint arXiv:2402.17360*, 2024.
- [12] X. Li, H. Wang, L. Yi, L. J. Guibas, A. L. Abbott, and S. Song, "Category-level articulated object pose estimation," in *Proceedings of the IEEE/CVF conference on computer vision and pattern recognition*, 2020, pp. 3706–3715.
- [13] A. Kirillov, E. Mintun, N. Ravi, H. Mao, C. Rolland, L. Gustafson, T. Xiao, S. Whitehead, A. C. Berg, W.-Y. Lo *et al.*, "Segment anything," in *Proceedings of the IEEE/CVF International Conference on Computer Vision*, 2023, pp. 4015–4026.
- [14] X. Wang, X. Zhang, Y. Cao, W. Wang, C. Shen, and T. Huang, "Seggpt: Towards segmenting everything in context," in *Proceedings of the IEEE/CVF International Conference on Computer Vision*, 2023, pp. 1130–1140.
- [15] L. Ke, M. Ye, M. Danelljan, Y.-W. Tai, C.-K. Tang, F. Yu *et al.*, "Segment anything in high quality," *Advances in Neural Information Processing Systems*, vol. 36, 2024.
- [16] J. Zhang, C. Bai, H. He, W. Xia, Z. Wang, B. Zhao, X. Li, and X. Li, "Sam-e: Leveraging visual foundation model with sequence imitation for embodied manipulation," *arXiv preprint arXiv:2405.19586*, 2024.
- [17] S. Huang, I. Ponomarenko, Z. Jiang, X. Li, X. Hu, P. Gao, H. Li, and H. Dong, "Manipvqa: Injecting robotic affordance and physically grounded information into multi-modal large language models," *arXiv preprint arXiv:2403.11289*, 2024.
- [18] T. Brown, B. Mann, N. Ryder, M. Subbiah, J. D. Kaplan, P. Dhariwal, A. Neelakantan, P. Shyam, G. Sastry, A. Askell *et al.*, "Language models are few-shot learners," *Advances in neural information processing systems*, vol. 33, pp. 1877–1901, 2020.
- [19] H. Touvron, T. Lavril, G. Izacard, X. Martinet, M.-A. Lachaux, T. Lacroix, B. Rozière, N. Goyal, E. Hambro, F. Azhar *et al.*, "Llama: Open and efficient foundation language models," *arXiv preprint arXiv:2302.13971*, 2023.
- [20] A. Guo, B. Wen, J. Yuan, J. Tremblay, S. Tyree, J. Smith, and S. Birchfield, "Handal: A dataset of real-world manipulable object categories with pose annotations, affordances, and reconstructions," in *2023 IEEE/RSJ International Conference on Intelligent Robots and Systems (IROS)*. IEEE, 2023, pp. 11 428–11 435.
- [21] H. Luo, W. Zhai, J. Zhang, Y. Cao, and D. Tao, "Learning affordance grounding from exocentric images," in *Proceedings of the IEEE/CVF conference on computer vision and pattern recognition*, 2022, pp. 2252–2261.
- [22] A. Nguyen, D. Kanoulas, D. G. Caldwell, and N. G. Tsagarakis, "Object-based affordances detection with convolutional neural networks and dense conditional random fields," in *2017 IEEE/RSJ International Conference on Intelligent Robots and Systems (IROS)*. IEEE, 2017, pp. 5908–5915.
- [23] F. Xiang, Y. Qin, K. Mo, Y. Xia, H. Zhu, F. Liu, M. Liu, H. Jiang, Y. Yuan, H. Wang *et al.*, "Sapient: A simulated part-based interactive environment," in *Proceedings of the IEEE/CVF conference on computer vision and pattern recognition*, 2020, pp. 11 097–11 107.
- [24] J. Deng, W. Dong, R. Socher, L.-J. Li, K. Li, and L. Fei-Fei, "Imagenet: A large-scale hierarchical image database," in *2009 IEEE conference on computer vision and pattern recognition*. Ieee, 2009, pp. 248–255.
- [25] T.-Y. Lin, M. Maire, S. Belongie, J. Hays, P. Perona, D. Ramanan, P. Dollár, and C. L. Zitnick, "Microsoft coco: Common objects in context," in *Computer Vision—ECCV 2014: 13th European Conference, Zurich, Switzerland, September 6–12, 2014, Proceedings, Part V 13*. Springer, 2014, pp. 740–755.
- [26] A. Kuznetsova, H. Rom, N. Alldrin, J. Uijlings, I. Krasin, J. Pont-Tuset, S. Kamali, S. Popov, M. Mallocci, A. Kolesnikov *et al.*, "The open images dataset v4: Unified image classification, object detection, and visual relationship detection at scale," *International journal of computer vision*, vol. 128, no. 7, pp. 1956–1981, 2020.
- [27] A. Ismail, S. A. Ahmad, A. C. Soh, M. K. Hassan, and H. H. Harith, "Mynursinghome: A fully-labelled image dataset for indoor object classification," *Data in Brief*, vol. 32, p. 106268, 2020.
- [28] Pixabay, "Pixabay.com," 2010, accessed: 2024-08-15.
- [29] CVAT.ai, "Cvat: Computer vision annotation tool," 2017, accessed: 2024-08-14.
- [30] A. Dosovitskiy, "An image is worth 16x16 words: Transformers for image recognition at scale," *arXiv preprint arXiv:2010.11929*, 2020.
- [31] L. Mur-Labadia, R. Martinez-Cantin, and J. J. Guerrero, "Bayesian deep learning for affordance segmentation in images," in *2023 IEEE International Conference on Robotics and Automation (ICRA)*. IEEE, 2023, pp. 6981–6987.
- [32] X. Lai, Z. Tian, Y. Chen, Y. Li, Y. Yuan, S. Liu, and J. Jia, "Lisa: Reasoning segmentation via large language model," in *Proceedings of the IEEE/CVF Conference on Computer Vision and Pattern Recognition*, 2024, pp. 9579–9589.
- [33] K. Mo, S. Zhu, A. X. Chang, L. Yi, S. Tripathi, L. J. Guibas, and H. Su, "Partnet: A large-scale benchmark for fine-grained and hierarchical part-level 3d object understanding," in *Proceedings of the IEEE/CVF conference on computer vision and pattern recognition*, 2019, pp. 909–918.
- [34] C. Zhong, Y. Zheng, Y. Zheng, H. Zhao, L. Yi, X. Mu, L. Wang, P. Li, G. Zhou, C. Yang *et al.*, "3d implicit transporter for temporally consistent keypoint discovery," in *Proceedings of the IEEE/CVF International Conference on Computer Vision*, 2023, pp. 3869–3880.